



THIS MANUSCRIPT HAS BEEN SUBMITTED TO THE ANNALS OF GLACIOLOGY AND HAS NOT BEEN PEER-REVIEWED.

### On sea ice emission modeling for MOSAiC's L-band radiometric measurements

Journal:	<i>Annals of Glaciology</i>
Manuscript ID	AOG-92-0449
Manuscript Type:	Article
Date Submitted by the Author:	20-Dec-2023
Complete List of Authors:	Hernández-Macià, Ferran; Institute of Marine Sciences; IsardSAT, Gabarro, Carolina; Institute of Marine Sciences Huntemann, Marcus; University of Bremen, Institute of Environmental Physics Naderpour, Reza; Sonova Holding AG Johnson, Joel; The Ohio State University, ElectroSciences Laboratory Jezek, Kenneth; The Ohio State University
Keywords:	Sea ice, Remote sensing, Sea-ice modelling, Sea-ice geophysics
Abstract:	The sea ice thickness retrieval using L-band passive remote sensing requires robust sea ice emission models. In this work, measurements from surface-based radiometers during MOSAiC are assessed with the Burke, Wilheit and SMRT models. These models encompass three distinct methodologies: incoherent without scattering, incoherent with scattering, and coherent approaches. Before running them, the sea ice growth is simulated using the CFDD model to further compute the evolution during each period. Ice cores near the instruments are used as initial state of the computation, along with DTC data to derive the sea ice temperature. The results suggest that the coherent approach used in the Wilheit model results in a better agreement with the horizontal polarization of the in situ measured brightness temperature. The Burke and SMRT incoherent models offer a more robust fit for the vertical component. These models are almost equivalent since the scattering considered in SMRT can be safely neglected at this low frequency, but the Burke model misses an important contribution from the snow layer above sea ice. The results also suggest that a more realistic permittivity falls between the spheres and random needles formulations, with potential for refinement, particularly for L-band applications, through future field measurements.



SCHOLARONE™  
Manuscripts

# On sea ice emission modeling for MOSAiC's L-band radiometric measurements

Ferran HERNÁNDEZ-MACIÀ<sup>1,2</sup>, Carolina GABARRÓ<sup>1</sup>, Marcus HUNTEMANN<sup>3</sup>, Reza NADERPOUR<sup>4</sup>, Joel T. JOHNSON<sup>5</sup>, and Ken C. JEZEK<sup>5</sup>

<sup>1</sup>*Barcelona Expert Center (BEC), Institute of Marine Sciences (ICM-CSIC), Barcelona, Spain*

<sup>2</sup>*isardSAT, Barcelona*

<sup>3</sup>*University of Bremen, Institute of Environmental Physics, Bremen, Germany*

<sup>4</sup>*Sonova AG, Staefa, Switzerland*

<sup>5</sup>*The Ohio State University, Columbus, OH USA*

*Correspondence: Ferran Hernández-Macià <fhernandezmacia@icm.csic.es>*

**ABSTRACT.** The retrieval of sea ice thickness using L-band passive remote sensing requires robust models for emission from sea ice. In this work, measurements obtained from surface-based radiometers during the MOSAiC expedition are assessed with the Burke, Wilheit and SMRT radiative transfer models. These models encompass three distinct methodologies: incoherent without scattering, incoherent with scattering, and coherent approaches. Before running these emission models, the sea ice growth is simulated using the Cumulative Freezing Degree Days (CFDD) model to further compute the evolution of the ice structure during each period. Ice coring profiles done near the instruments are used to obtain the initial state of the computation, along with Digital Thermistor Chain (DTC) data to derive the sea ice temperature during the analyzed periods. The results suggest that the coherent approach used in the Wilheit model results in a better agreement with the horizontal polarization of the in situ measured brightness temperature. The Burke and SMRT incoherent models offer a more robust fit for the vertical component. These models are almost equivalent since the scattering considered in SMRT can be safely neglected at this low frequency, but the Burke model misses

28        **an important contribution from the snow layer above sea ice. The results**  
29        **also suggest that a more realistic permittivity falls between the spheres and**  
30        **random needles formulations, with potential for refinement, particularly for**  
31        **L-band applications, through future field measurements.**

## 32 1 INTRODUCTION

33 From September 2019 to October 2020, the Multidisciplinary drifting Observatory for the Study of Arctic  
34 Climate (MOSAiC) expedition presented an exceptional chance to gather data on sea ice characteristics  
35 over the course of an entire year (Nicolaus and others (2022)). In October 2019, the Polarstern anchored  
36 itself to an ice floe spanning approximately 2.8 km x 3.8 km in the northern region of the Laptev Sea.  
37 To perform an extensive range of measurements from various research teams, a dedicated science camp  
38 was established on the drifting ice floe. This expedition offered a unique opportunity to investigate the  
39 variability of the sea ice microwave emissivity signature due to seasonal fluctuations, temperature changes,  
40 and the shift from melting to freezing periods. In this work, the ETH L-Band Radiometer (ELBARA,  
41 Schwank and others (2010)) and the Ultra Wideband Microwave Radiometer (UWBRAD, Johnson and  
42 others (2016)) measurements in autumn and winter are analyzed, both being radiometers designed to mea-  
43 sure statically due to their size.

44  
45        When considering frequencies below 2 GHz, the electromagnetic waves can penetrate the sea ice column  
46 to a significant depth (Heygster and others (2014)). This level of penetration permits low-frequency ra-  
47 diometers to capture emissions from deeper layers of the ice, including emission from the ocean, compared  
48 to higher frequency radiometers like the Advanced Microwave Scanning Radiometer-2 (AMSR-2). Conse-  
49 quently, lower frequency instruments can be utilized to measure the thickness of thin sea ice. Specifically,  
50 at L-band (1.4 GHz), the sensitivity to ice thickness typically is within the range of 50 cm to 1 m, de-  
51 pending on the salinity and temperature of the ice (Kaleschke and others (2012); Maass and others (2015);  
52 Huntemann and others (2014); Demir and others (2022b)). The utilization of L-band radiometry proves  
53 to be an excellent tool for monitoring the thickness of Arctic sea ice due to a significant proportion of the  
54 Arctic ice being seasonal and relatively thin, amounting to approximately 70% covering in January (Kwok  
55 (2018)). Several satellites are designed for observing passive microwave emission at L-band, such as the

56 ESA's Soil Moisture and Ocean Salinity (SMOS) satellite (Mecklenburg and others (2009); Font and others  
57 (2010); Kerr and others (2010)), the NASA's Soil Moisture Active Passive (SMAP) satellite (Entekhabi  
58 and others (2010)), or the Aquarius carried on the Satélite de Aplicaciones Científicas - D (SAC-D) satellite.

59

60 Many radiative transfer models can be used to compute the brightness temperature (TB) of sea ice,  
61 and important differences appear when using one or another. In this work three different approaches are  
62 analyzed: the Burke model (Burke and others (1979)), which neglects coherence effects and scattering; the  
63 SMRT model (Picard and others (2018)), which neglects coherence but considers scattering; and the Wilheit  
64 model (Wilheit (1978)), which uses an coherent approach but neglecting scattering. Another key parameter  
65 that determines the brightness temperature is the selection of the sea ice permittivity formulation. The most  
66 widely used is the Vant empirical formulation (Vant and others (1978)), but another and more theoretical  
67 approach which models the brine inclusions as ellipsoids is described in Shokr (1998). In this paper, the  
68 different model predictions are compared to measured data to better understand how improvements to sea  
69 ice thickness can be achieved.

## 70 **2 DATA COLLECTION AND MANAGEMENT**

71 ELBARA and UWBRAD data collected during the MOSAiC expedition is analyzed throughout this work.  
72 These instruments measured during distinct times and at varying locations, which in turn allows analyzing  
73 various situations. For the sea ice growth simulation ancillary in situ measurements required.

### 74 **2.1 ELBARA**

75 ELBARA is an instrument to measure L-band thermal emission (Schwank and others (2010)). For the  
76 MOSAiC expedition, it was mounted on a sledge and equipped with a picket-horn antenna and a manual  
77 elevation positioner. This antenna has a Field of View (FoV) of  $\pm 23^\circ$  at  $-3$  dB sensitivity relative to  
78 the boresite pointing at nadir observation angle  $\theta$ . Because the antenna temperature  $T_B^p(\theta)$  measured at  
79 horizontal or vertical polarizations deviates from the brightness temperature of the central facet of the  
80 footprint, a conversion is used to obtain a representative brightness temperature of the observed footprint.  
81 The methodology to perform this conversion and the calibration procedures is described in Naderpour and  
82 Schwank (2021).

83 During the MOSAiC expedition, a total of 25904 measurements were collected by ELBARA. They cor-

84 respond to observations during various periods, with a nominal off-nadir angle of  $60^\circ$  and a temporal  
85 resolution of 5 minutes. Each day's data is averaged in order to obtain a day-by-day evolution comparable  
86 to the sea ice growth simulation models.

87 ELBARA observations occurred in the MOSAiC's Remote Sensing (RS) site over three periods: October  
88 29th through November 20th, December 2nd to the 13th, and December 22nd to 30th.

## 89 **2.2 UWBRAD**

90 UWBRAD is an instrument that observes sea ice microwave emissions at four different frequencies (540,  
91 900, 1380, and 1740 MHz) across the spectrum range of 0.5-2 GHz (Johnson and others (2016)). The  
92 instrument operates with right-hand, circular polarization. Each frequency has a bandwidth of 125 MHz  
93 and 512 sub-channels, with data samples generated every four seconds for 100 ms antenna observation  
94 time. The lowest frequency is more sensitive to deeper ice layers than L-band radiometers, allowing  
95 for more accurate thickness estimations (Demir and others (2022a)). Additionally, UWBRAD utilizes a  
96 Radio Frequency Interference (RFI) mitigation algorithm to remove unwanted signals, allowing operation  
97 in unprotected bands.

98 The instrument was deployed on the ice at the Remote Sensing (RS) site and performed measurements  
99 over two periods, on December 4 – 13, 2019 (Demir and Johnson (2021a)), and January 17 – 23, 2020  
100 (Demir and Johnson (2021b)). It monitored the sea ice in configurable oblique angles (35 – 50 off-nadir) to  
101 measure thermal emission signatures at the different sensor frequencies. The instrument was positioned on  
102 a stationary telescoping mast, offering the flexibility to manually adjust its height as needed. The antenna's  
103 orientation was precisely controlled by a programmable rotator unit, enabling the monitoring of sea ice  
104 from a specified oblique angle. Additionally, this setup facilitated periodic sky measurements for 5 out of  
105 every 15 minutes. After the expedition, algorithms for detecting and mitigating RFI were applied to data to  
106 eliminate undesired signals from the data collected. The Level 1 data underwent both internal calibration  
107 using a noise diode and external calibration utilizing sky measurements, resulting in the processing of the  
108 data to Level 2 and Level 3, respectively. In the last phase of data processing, the Level 3 data underwent  
109 a smoothing procedure by applying a 100-sample running average. As for ELBARA, UWBRAD data of  
110 each day was averaged in order to obtain the day-by-day evolution in the comparison with the modeled  
111 outputs.

112 Measurements of the sea ice internal temperature and salinity profiles, basal growth rates, and snow layer

MOSAiC's event code	Date	MOSAiC's event code	Date	MOSAiC's event code	Date
<i>PS122/1_4-29</i>	2019-10-24	<i>PS122/1_7-78</i>	2019-11-14	<i>PS122/1_11-11</i>	2019-12-10
<i>PS122/1_5-24</i>	2019-10-30	<i>PS122/1_8-22</i>	2019-11-19	<i>PS122/2_15-12</i>	2019-12-15
<i>PS122/1_6-61</i>	2019-11-07	<i>PS122/1_10-39</i>	2019-12-04	<i>PS122/2_20-92</i>	2020-01-18

**Table 1.** Overview of the BGC1 ice cores used in the work.

113 thickness were made by other members of the MOSAiC expedition. The sea ice for the UWBRAD study  
 114 was characteristic of undeformed, low salinity, second-year ice that was potentially a refrozen melt pond.  
 115 The ice was covered by a 5-15 cm thick layer of undisturbed snow.

### 116 2.3 Ice coring and DTC profiles

117 In this work, ice cores taken nearby are used, as only a few ice cores were performed in the RS site where the  
 118 radiometers were deployed. Specifically, the cores from the BioGeoChemistry-1 (BGC1) site (Angelopoulos  
 119 and others (2022)) are selected, as they were obtained periodically from a nearby location. An overview of  
 120 the ice cores used in this work can be found in Table 1. The BGC1 site corresponds to a first-year ice zone  
 121 that is suspected to have formed from open seawater around October 2019. This may be distinct in some  
 122 aspects from the mid December RS site ice as described in Demir and others (2022a). However, where  
 123 necessary, the potential impact of this distinction is discussed and addressed.

124 Aside from the ice coring profiles, information from digital thermistor chains (DTC) are used to derive  
 125 the sea ice temperature evolution, and also as a check for the sea ice thickness simulation from CFDD.  
 126 Concretely, the DTC12 (Salganik and others (2023a)) is used for the first ELBARA period, and the DTC20  
 127 (Salganik and others (2023b)) for the rest of the periods.

## 128 3 MODELING

### 129 3.1 Sea ice growth evolution: Cumulative Freezing Degree Days

The Cumulative Freezing Degree Days (CFDD) model is an empirical formulation (Bilello (1961); Weeks  
 (2010)) which allows computing sea ice thickness growth, based on the following equation:

$$d_{ice} = 1.33(CFDD)^{0.58}, \quad (1)$$

where the obtained ice thickness is in cm. The CFDD variable corresponds to the daily average 2 m air temperature difference with respect to the seawater freezing point of  $T_w = -1.8^\circ\text{C}$ .

To simulate the sea ice temperature ( $T_{ice}$ ) along the time evolution, a linear gradient is assumed as a reasonable approximation following Huntemann (2015). Therefore, using the 2 m air temperature ( $T_{2m}$ ) obtained from the European Centre for Medium-Range Weather Forecasts (ECMWF) Reanalysis v5 (ERA5, Hersbach and others (2020)) model, the ice bulk temperature can be computed:

$$T_{ice} = \frac{T_{2m} - T_w}{2}. \quad (2)$$

Regarding the sea ice salinity ( $S_{ice}$ ), an empirical relation from Nakawo and Sinha (1981) is utilized:

$$S_{ice} = \frac{0.12S_w}{0.12 + 0.88e^{-4.2 \times 10^{-4}v}}, \quad (3)$$

130 where  $S_w = 33$  is a typical Arctic seawater salinity, and  $v$  is the growth rate computed from the simulation  
131 itself.

### 132 3.2 Radiative transfer models

133 In this section, three radiative transfer models to compute the brightness temperature, given the permit-  
134 tivity and the conditions of the ice and snow, are presented. The Burke and SMRT models are based on  
135 an incoherent approach, while the Wilheit model accounts for the phase of the electromagnetic waves, i.e.  
136 it considers coherence effects. However, while the Burke and Wilheit models neglect scattering, the SMRT  
137 model does not.

138 For all the models only four layers are considered: air - snow - ice - water, with the first and the last con-  
139 sidered to be semi-infinite. Various conditions are used as inputs, including sea ice thickness, temperature,  
140 and salinity. The sea ice temperature and salinity values determine the permittivity, and are also used as  
141 input parameters. The snow layer is assumed to be isothermal with the underlying ice layer, non-saline,  
142 and a thickness equivalent to 10% of the ice thickness (Doronin (1971)). Lastly, the seawater is treated  
143 as a semi-infinite layer and is assumed to have typical Arctic values, with a temperature of  $-1.8^\circ\text{C}$  and a  
144 salinity of 33.



### 145 3.2.1 Burke model

146 The Burke model is based on a radiative transfer model initially presented in Burke and others (1979) for  
147 soil microwave emissivity. This model operates under the assumption of the radiation incoherent approach.  
148 Moreover, it assumes the absence of emission and attenuation of the atmosphere, and considers that the  
149 sky has an isotropic brightness temperature of 5 K. Furthermore, it assumes homogeneity within the layers,  
150 with constant permittivity, temperature, and salinity throughout each layer. It also assumes smooth surface  
151 layers. Following the derivation described in Burke and others (1979), the modeled brightness temperature  
152 in a given polarization is a combination of the radiation emitted by the layered structure and the radiation  
153 reflected by the sky. This approach was already used with ARIEL data in Gabarró and others (2022),  
154 being successful in studying the instrument sensitivity to sea ice emission.

### 155 3.2.2 Wilheit model

156 Another option to model the emission of sea ice at L-band is the one based in Wilheit (1978), also originally  
157 designed for soil. The main difference with Burke's is that this model does not neglect coherence effects,  
158 and also that it naturally considers an infinite number of reflections within the layers. This behavior can  
159 occur at low frequencies if there are two or more interfaces in a plane-parallel media, as an electromagnetic  
160 plane wave has the ability to interact with its reflected counterpart interfering between them. As discussed  
161 in Huntemann and others (2014), coherence can be particularly significant in the presence of a thin snow  
162 layer above ice. However it is noted that roughness on any interface (air-snow, snow-ice, or ice-water) can  
163 rapidly reduce coherent interactions, such that many past studies have failed to show evidence of significant  
164 coherent interactions (Jezek and others (2019)).

### 165 3.2.3 SMRT model

166 The Snow Microwave Radiative Transfer (SMRT) thermal emission and backscatter model offers a variety  
167 of configuration options in computing microwave emission (Picard and others (2018)). This flexibility  
168 allows choosing between different electromagnetic theories, snow and sea ice microstructure and others. It  
169 is a radiative transfer model so the layer interferences and coherence effects are neglected, and it considers  
170 the layers as plane-parallel, horizontally infinite and homogeneous. In this work, SMRT is run selecting  
171 the IBA scattering, along with the Polder-von Santen mixing formula considering two types of inclusions:  
172 random needles or spheres inclusion for the sea ice permittivity.

### 173 **3.3 Permittivity modeling**

#### 174 *3.3.1 Empirical formulation*

175 In Vant and others (1978), a linear relationship between the brine volume fraction and the complex dielectric  
176 constant is empirically established, and this relationship holds for both first-year and multi-year sea ice.  
177 These empirical coefficients can be interpolated to the desired frequency band, in this case 1.4 GHz.

#### 178 *3.3.2 Theoretical formulation*

179 A more theoretical approach considers sea ice as a combination of two dielectric materials: ice and brine.  
180 The configuration and orientation of brine inclusions within the mixture, plays a significant role, as studied  
181 by Shokr (1998). Two inclusion shapes are examined in this work: spherical inclusions and randomly  
182 oriented needle-like inclusions. Harsh conditions during ice formation may result in randomly oriented  
183 needle-like inclusions, while smoother conditions with minimal temperature fluctuations can lead to spher-  
184 ical inclusions or vertically oriented needles or ellipsoids (Shokr (1998), Vant and others (1978)). As the  
185 ice gets colder, the brine's salinity increases. Therefore, in empirical models, the salinity is often repre-  
186 sented as a polynomial function of temperature (Assur (1960)). Regarding the dielectric mixing formulas,  
187 the complex dielectric constants of pure ice and brine are necessary. The dielectric constant of pure ice  
188 is dependent on temperature and frequency and can be modeled using the approach described in Mät-  
189 zler (2006), even though in the given frequency range of observations, the modeled permittivity does not  
190 change noticeably based on frequency. On the other hand, the dielectric constant of brine is obtained from  
191 Stogryn and Desargant (1985). When considering pure ice as the host material and the brine as well as  
192 the inclusions, the expressions for the two types of sea ice inclusions are derived from Shokr (1998).

#### 193 *3.3.3 Properties*

194 Figure 1 shows the 1.4 GHz brightness temperature as a function of the sea ice thickness for the three  
195 presented formulations. There is a clear difference among the three dielectric models, and also between  
196 the three radiative transfer models, when it comes to the relationship between the TB and the thickness  
197 of sea ice. In certain cases, this difference can be as high as 50 K. The reason behind this contrast can be  
198 understood by examining the analysis provided in Huntemann (2015). These permittivity models can be  
199 categorized into three groups based on their levels of absorption: high absorption, moderate absorption,

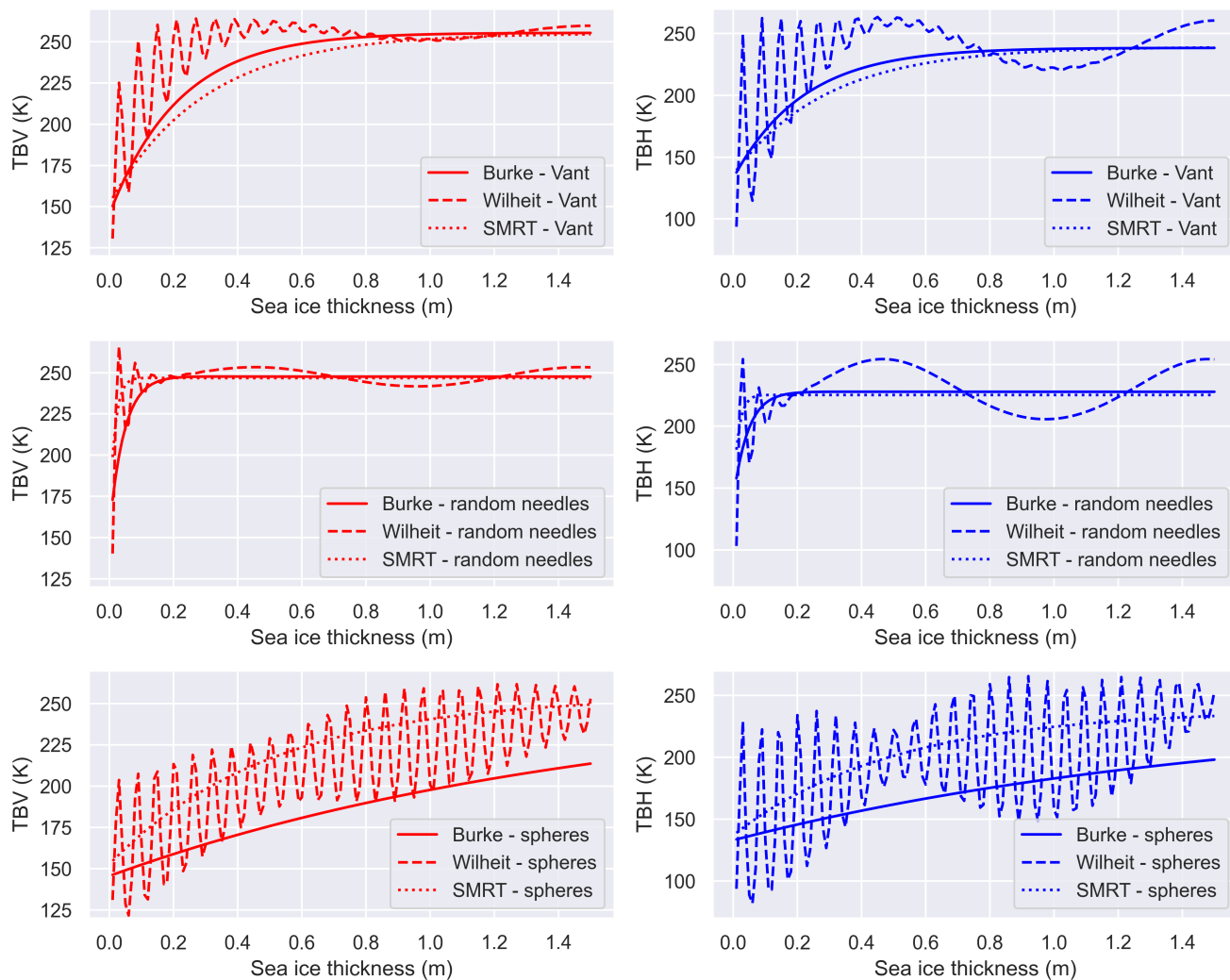


**Fig. 1.** 1.4 GHz brightness temperature as a function of the sea ice thickness, assuming fixed sea ice conditions ( $T_{ice} = -10^{\circ}C$ ,  $S_{ice} = 10$ ), for the three radiative transfer models assuming the three presented sea ice permittivity formulations.

200 and low absorption. The high absorption category is assigned to the random needles model, which exhibits  
201 early saturation and emission primarily influenced by surface conditions. The Vant formulation falls under  
202 the moderate absorption category due to its lower saturation and intermediate status. The spheres model  
203 is classified as having low absorption because it does not reach saturation at high thickness levels.

204

205

206 The real part of the complex dielectric constant for the snow layer is obtained from Mätzler (1996),  
207 while the imaginary part is derived from Tiuri and others (1984) and Mätzler (2006). The formulation of  
208 the complex dielectric constant of the snow is dependent on its density, and a typical value of  $0.3 \text{ gcm}^{-2}$   
209 is commonly used for the Arctic region, as stated in Warren and others (1999). Additionally, the complex  
210 permittivity of seawater is acquired from Klein and Swift (1977), assuming a standard salinity value of 33  
211 for the Arctic Ocean.

## 212 4 RESULTS

213 ELBARA and UWBRAD data from MOSAiC are analyzed by comparing with model simulations. Prior to  
214 computing the microwave emission, the CFDD model is used to simulate the sea ice growth evolution. In  
215 many figures, the different models are named with abbreviations. To clarify it, it is noteworthy to mention  
216 that the different permittivities, i.e. Vant, random needles and spheres, are depicted by *vant*, *rn* and *sp*,  
217 respectively.

218 The first two MOSAiC legs took place during autumn of 2019. This period corresponds to sea ice con-  
219 tinuously growing. Therefore, static measurements from the L-band radiometers deployed in the ice floe  
220 can be compared to the CFDD simulation, which require in situ sea ice conditions derived from ice coring  
221 activities, combined with a radiative transfer model to compute the emitted brightness temperature. How-  
222 ever, to double-check the conducted simulation, DTC measurements are used to obtain information on the  
223 sea ice thickness and temperature evolution during the analyzed periods.

### 224 4.1 Sea ice growth simulation: late 2019 and early 2020

225 Figure 2 shows how the modeled sea ice conditions, thickness, temperature and salinity, evolve during  
226 the sea ice growth period until late 2019, along with data from the BGC1 ice coring and DTC profiles.  
227 Hereafter, the label CFDD refers to the simulation described in section 3.1, where the sea ice thickness

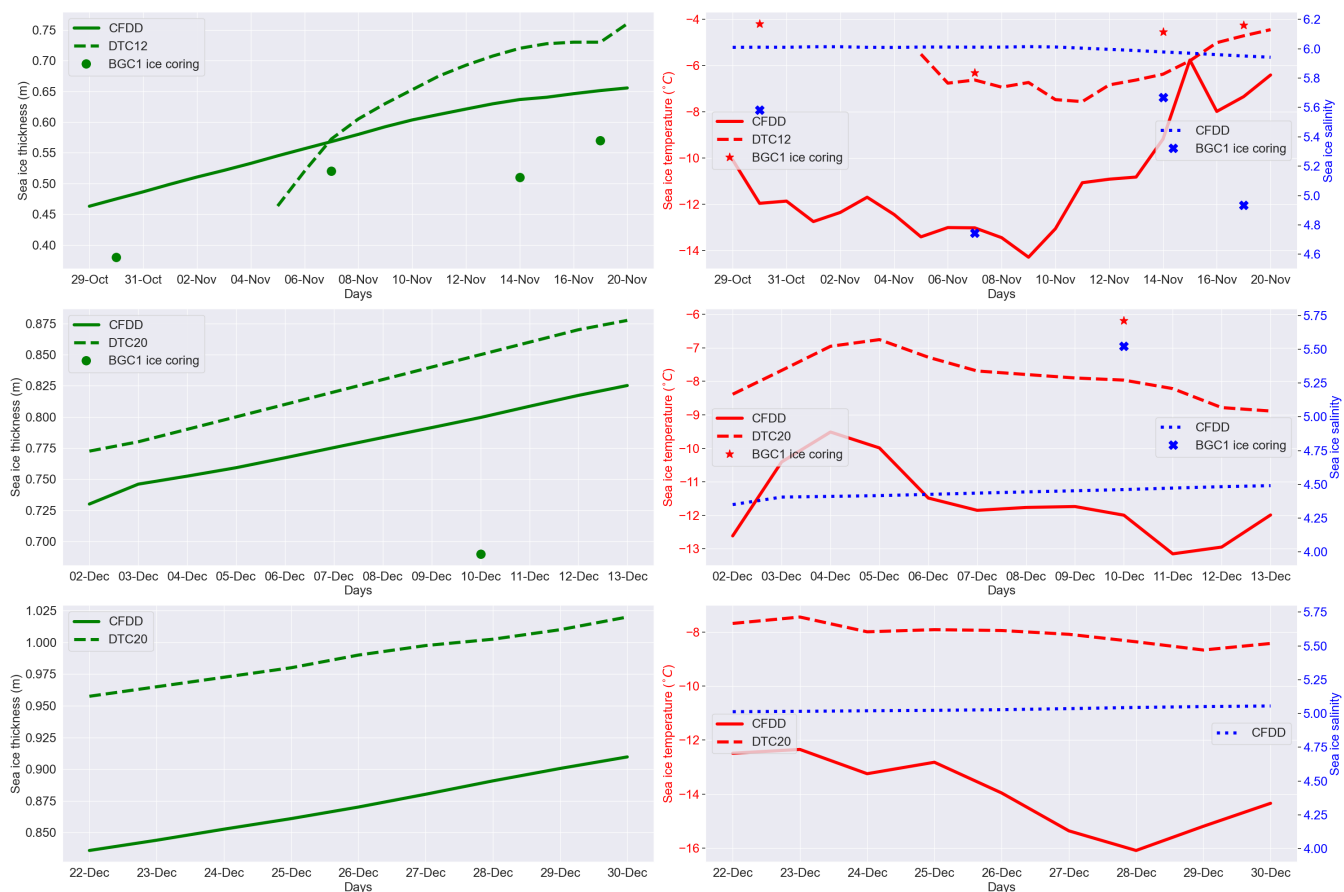


**Fig. 2.** Temporal evolution of the sea ice conditions modeled with the CFDD model during late autumn and early winter 2019/2020 of MOSAiC, along with in situ conditions extracted from BGC1 ice cores and DTC measurements.

228 is computed with the CFDD model itself, the sea ice temperature from the linear gradient assumption  
229 using the meteorological data, and the sea ice salinity from the Nakawo and Sinha (1981) formulation.  
230 The CFDD simulation is started, for the first period, from the sea ice temperature and salinity conditions  
231 extracted from the BGC1 ice core measured on October 24 2019. For the second period, the ice core from  
232 December 4 2019 is taken. Finally, for the last period the ice coring performed on December 15 2019 is  
233 used. This explains why there is a slight deviation in the sea ice temperature and salinity between the end  
234 and the start of the next simulated period.

235 As expected, the sea ice thickness keeps growing during this time, shown by both the ice coring and the  
236 DTC data, also well reproduced by the CFDD model. Regarding the temperature, it reproduces a general  
237 decrease in sea ice temperature as freeze-up advances. However, there is a major deviation of the linear  
238 gradient assumption taking the 2 m air temperature data from ERA5. This effect can be produced by  
239 the snow layer above (Maass and others (2015)), as it insulates the ice preventing it to reach lower tem-  
240 peratures as those obtained in the CFDD simulation. There is almost no variation through time of the  
241 sea ice layer averaged salinity reproduced with the Nakawo and Sinha (1981) formulation, despite a subtle  
242 increase observed in early December. This happens because the used formulation determines the salinity  
243 of the ice that has grown within a given period, so an stable growth rate such as the observed can produce  
244 it.

245 The sea ice conditions extracted from BGC1 ice cores that were measured throughout these periods, and  
246 the DTC installed near the RS site, are also shown in 2. For the latter, the sea ice thickness is derived  
247 directly from the difference between the snow-ice and the ice-water interfaces provided in Salganik and  
248 others (2023a) and Salganik and others (2023b). Regarding the DTC sea ice temperature, the bulk value is  
249 obtained by averaging all the temperatures measured by the thermistor chain sensors within the ice layer.  
250 During November, when sea ice is expected to be growing rapidly, four ice cores and the DTC12 are used  
251 as ground truth to study the reliability of the CFDD model. It seems to slightly overestimate the sea ice  
252 thickness compared to the ice cores, around 5 cm, but remains near the DTC-derived thickness with a  
253 similar general trend. Furthermore, there is a general underestimation compared to the DTC data, com-  
254 pared to both the DTC12 used in the first period and the DTC20 used in the rest, so the simulation lays  
255 in an intermediate region between the two in situ sources. Clear conclusions remain difficult because these  
256 ground truth data were not measured exactly where the radiometers were measuring, so this variable could  
257 be slightly different throughout the ice floe. However, for the sea ice temperature, the major deviation of

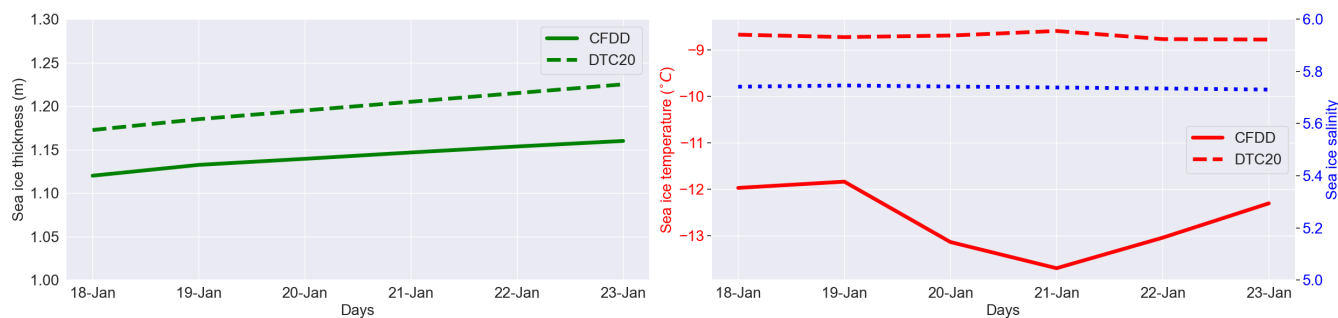


**Fig. 3.** **Left:** Temporal evolution of the sea ice thickness modeled with the CFDD model during mid January 2020, along with DTC measurements. **Right:** Temporal evolution of the sea ice temperature and salinity modeled with the CFDD model during mid January 2020, along with DTC measurements.

258 the CFDD simulation suggests the use of the sea ice temperature from the DTC's to compute the mod-  
 259 eled brightness temperature, which remain much near the ice coring profiles. Finally, the in situ salinity  
 260 measurements remain almost constant as also does the model, both around 5. This is further supported  
 261 by what is shown in Angelopoulos and others (2022), where a complete study of the MOSAiC's BGC  
 262 ice core data is presented. The sea ice evolution shown there indicates that the salinity had the typical  
 263 C-shape salinity profile (Cox and Weeks (1988)) in late October, i.e. a higher salinity at the top/bottom  
 264 and lower in the middle, which slowly changed into a less curved and saline profile. The average ice bulk  
 265 salinity remain mostly constant near 5, as also shows the Nakawo and Sinha (1981) model and the ice  
 266 coring profiles.

267 Therefore, in this work, the sea ice thickness and salinity from the CFDD simulation are combined with the  
 268 DTC-derived sea ice temperature to compute the modeled brightness temperature. It is remarkable that  
 269 the gap in the DTC12 data from October 29 to November 5 is filled by subtracting to the CFDD-simulated  
 270 temperature its mean difference with the DTC12 data, as they are shown to reproduce a similar trend.

271

272 Regarding the second period, during which UWBRAD was operational, 11 shows the temporal evolution  
 273 of the simulated sea ice conditions, using the BGC1 ice core from the January 18 2020 as initial state.  
 274 Unfortunately, no more ice cores were performed throughout this period, and thus no further insights  
 275 can be extracted. However, and similarly to the previous periods, the CFDD simulation is close to the  
 276 DTC-derived sea ice thickness, but presents a major deviation for the sea ice temperature, in this case  
 277 even showing a different trend. The model reproduces the expected trend for ice thicker than 1 m: a much  
 278 slower growth, less than a centimeter per day. For this period the modeled brightness temperature to be

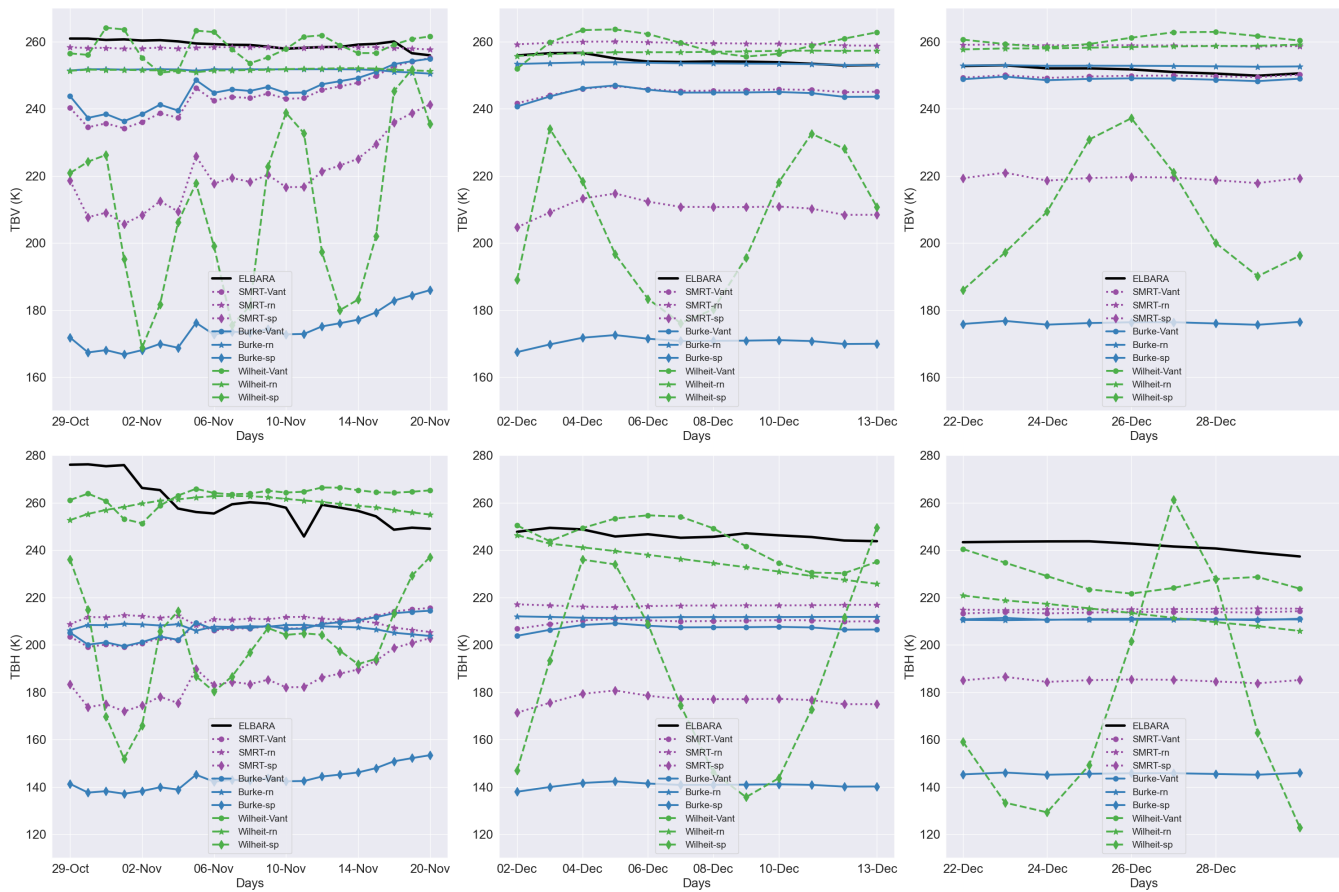


**Fig. 4.** Temporal evolution of brightness temperature, TBV on the upper row and TBH on the lower row, respectively, measured by ELBARA during the sea ice growth period, along with the model simulations.

279 compared with the in situ L-band radiometric data is computed using the same input sources: the sea ice  
 280 thickness and salinity from the CFDD simulation, along with the DTC-derived sea ice temperature.

## 281 4.2 Radiometric data analysis

282 The three radiative transfer models configured with the different ice permittivities are evaluated for the  
 283 sea ice growth period measurements of ELBARA and UWBRAD.

### 284 4.2.1 ELBARA measurements

285 The temporal evolution of the sea ice brightness temperature measured by ELBARA during the different  
 286 periods is shown in Fig. 4, along with the models output with the presented permittivities. The results  
 287 for the vertically-polarized brightness temperature (TBV) are better overall, as all the models considering  
 288 the Vant and the random needles permittivities have acceptable discrepancies with the observations. The



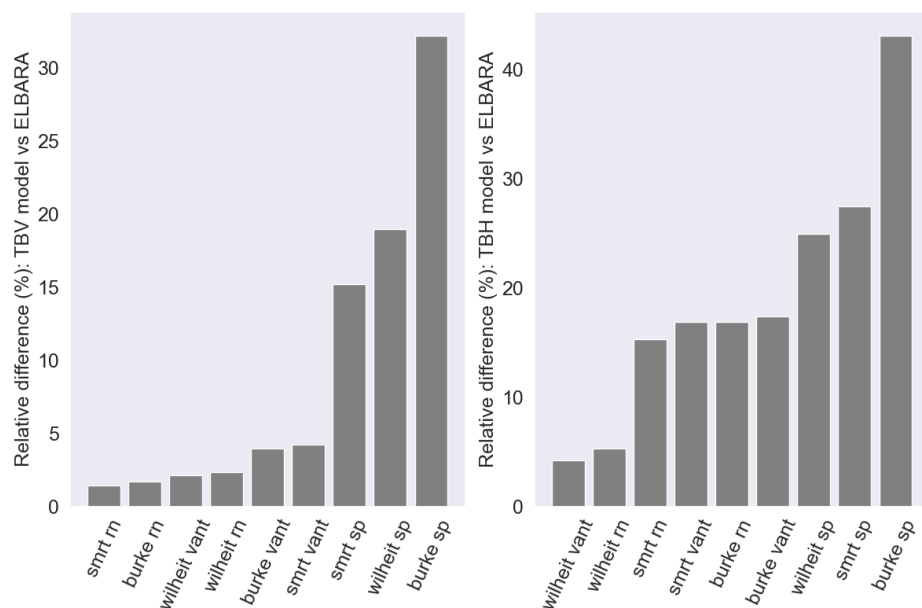


**Fig. 5.** **Left:** Relative difference of the modeled TBV from different models with respect to the in situ ELBARA measurements during the sea ice growth period. **Right:** Relative difference of the modeled TBH from different models with respect to the in situ ELBARA measurements during the sea ice growth period.

289 general trend is well reproduced by the models, although for the first days of the simulation there is a  
 290 deviation: the brightness temperature is slightly reduced while the models show an increase until stabilizing  
 291 around the measured values. This can arguably be because of the uncertainty introduced with the ice cores  
 292 taken as initial state. For the horizontally-polarized brightness temperature (TBH), in early November no  
 293 model is able to reproduce the large values measured by the sensor, which are not physically realistic for  
 294 sea ice with water underneath and may indicate a technical issue of the instrument or just RFI-corrupted  
 295 data. Only the Wilheit model, i.e. the coherent approach, can reach those unusually large measured  
 296 values, particularly with Vant's permittivity formulation, but not clear evidence of the oscillatory behaviors  
 297 predicted by the Wilheit model are present in the measured data. For the other periods, all the models  
 298 present a similar output, considerably lower than the in situ data. However, again the Wilheit model is  
 299 the closest as it exhibits higher values by including coherence effects.

300 Figure 5 shows the relative difference computed for each model configuration with respect to the ELBARA  
 301 measurements during the sea ice growth period, from late October to late December. The Burke and the  
 302 SMRT models present a similar behavior, as they are both incoherent and the scattering that is considered  
 303 at SMRT can be neglected at L-band. Nevertheless, the Burke model is generally lower than SMRT, as

304 also shown in 4, particularly when both models consider the Vant or the spheres formulations. Regarding  
305 the permittivity, the spherical brine inclusions produce a major difference for both polarizations. However,  
306 it is remarkable the combination with the Wilheit and SMRT models result in a better reproduction of  
307 the measured data. Focusing on TBV, the three permittivities almost sorted by relative difference with  
308 ELBARA are random needles, Vant, and spheres respectively, despite the radiative transfer model used.  
309 For TBH specifically, the relative metrics again indicate that the coherent model, combined with the Vant  
310 and the random needles models, are the best configurations to reach such large values.

311 Figure 6 provides scatter plots of different configurations compared to the in situ measurements, along with  
312 their  $R^2$  correlation coefficients. These plots highlight the similarity between the SMRT and the Burke  
313 models, which show nearly identical trends that are shifted to lower values for the Burke results. The Vant  
314 and the random needles formulations continue to generally present higher  $R^2$  values. Focusing on TBV,  
315 the correlation coefficients seem to be biased due to the in situ values above 257 K, as these points are  
316 clearly deviated compared to those that are lower. For the horizontal component, these plots confirm that  
317 only the Wilheit model is reasonable on getting closer to the ELBARA measurements, but little correlation  
318 is observed in the scatter plots.

#### 319 *4.2.2 UWBRAD measurements*

320 A similar analysis can be conducted for the 1380 MHz channel measurements of UWBRAD. It is remarkable  
321 that for every incidence angle at which UWBRAD conducted measurements during this period (see Fig.  
322 6 from Demir and others (2022a)), and because of the wideness of the UWBRAD antenna, its antenna  
323 pattern is projected onto the surface to get a range of observation angles and then the modeled sea ice  
324 brightness temperatures at the resulting varying incidence angles are integrated over the pattern. Figure  
325 7 shows the temporal evolution of the modeled brightness temperature and the in situ measurements  
326 from UWBRAD in early December. Every model is able to reproduce the subtle increasing trend on  
327 the brightness temperature measured by the instrument, although the Burke and the SMRT models are  
328 the best, except when assuming the spheres permittivity. Here the Burke and SMRT models present  
329 again an almost equivalent output, even though the latter shows a better agreement with the UWBRAD  
330 measurements, specially when considering the Vant formulation. Furthermore, in this case even the Wilheit  
331 model is capable of reproducing the increase on TB, but with more bias compared to the other radiative  
332 transfer models. It also does not show the oscillations observed in Figure 4.

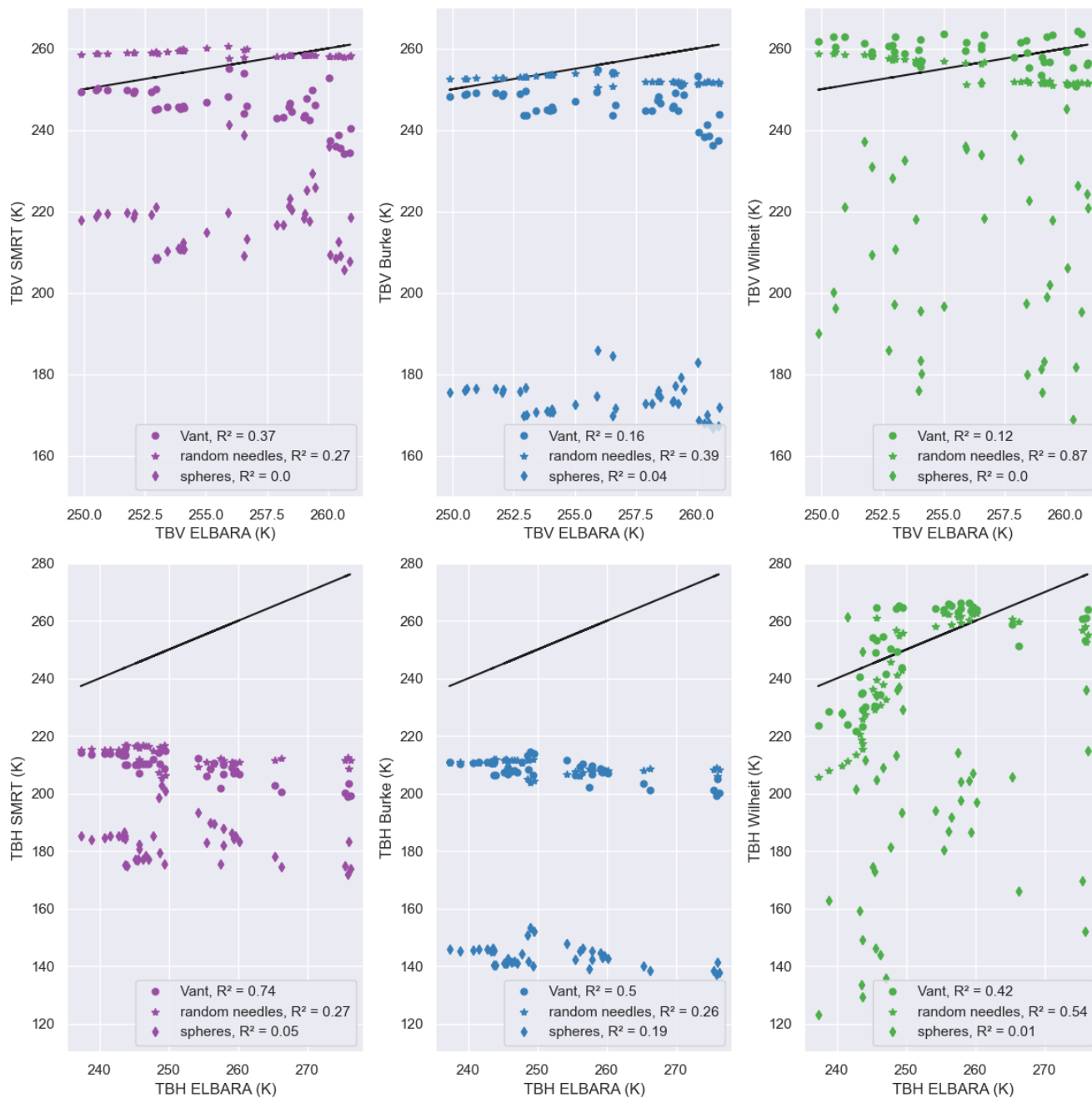


**Fig. 6.** Scatter plots of the brightness temperature modeled with the different configurations as function of the ELBARA measurements, along with their respective correlation coefficient, with TBV in the upper row and TBH in the lower row.

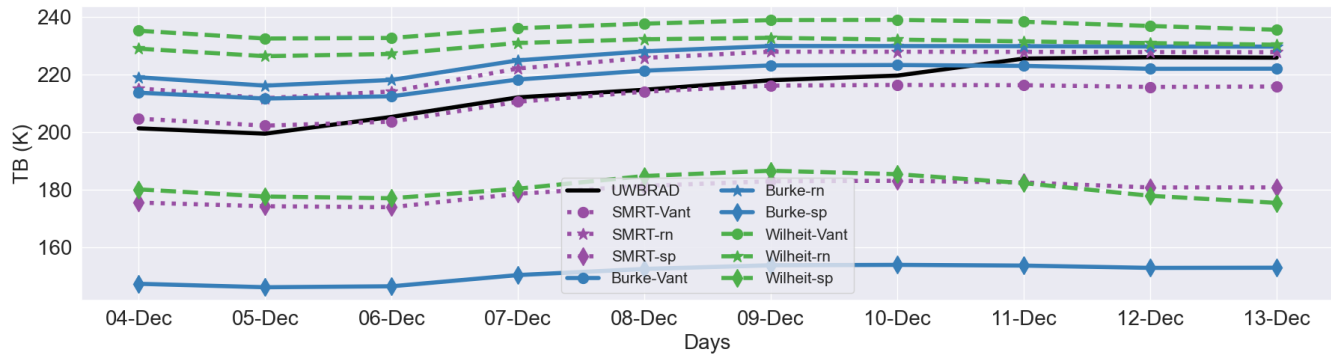


**Fig. 7.** Temporal evolution of the UWBRAD brightness temperature modeled with the combination of the CFDD simulation and the Burke, SMRT and Wilheit models, along with the UWBRAD's first period measurements.

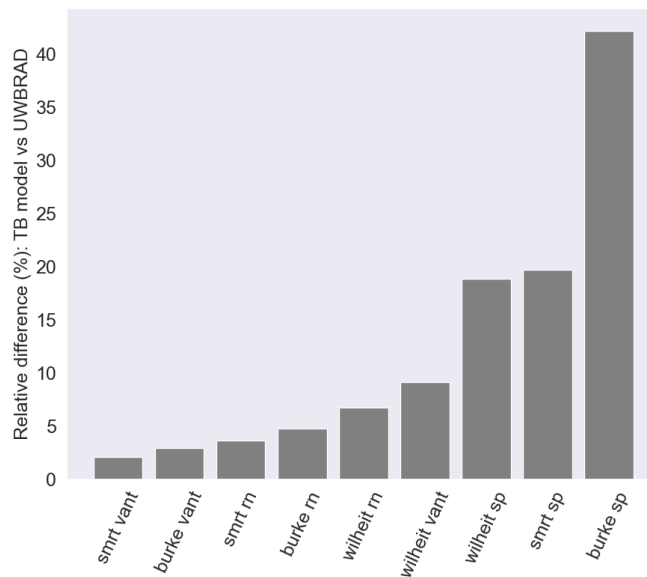


**Fig. 8.** Relative difference of the modeled brightness temperature from the Burke, SMRT and Wilheit models assuming different permittivities with respect to the in situ UWBRAD measurements during the first period.

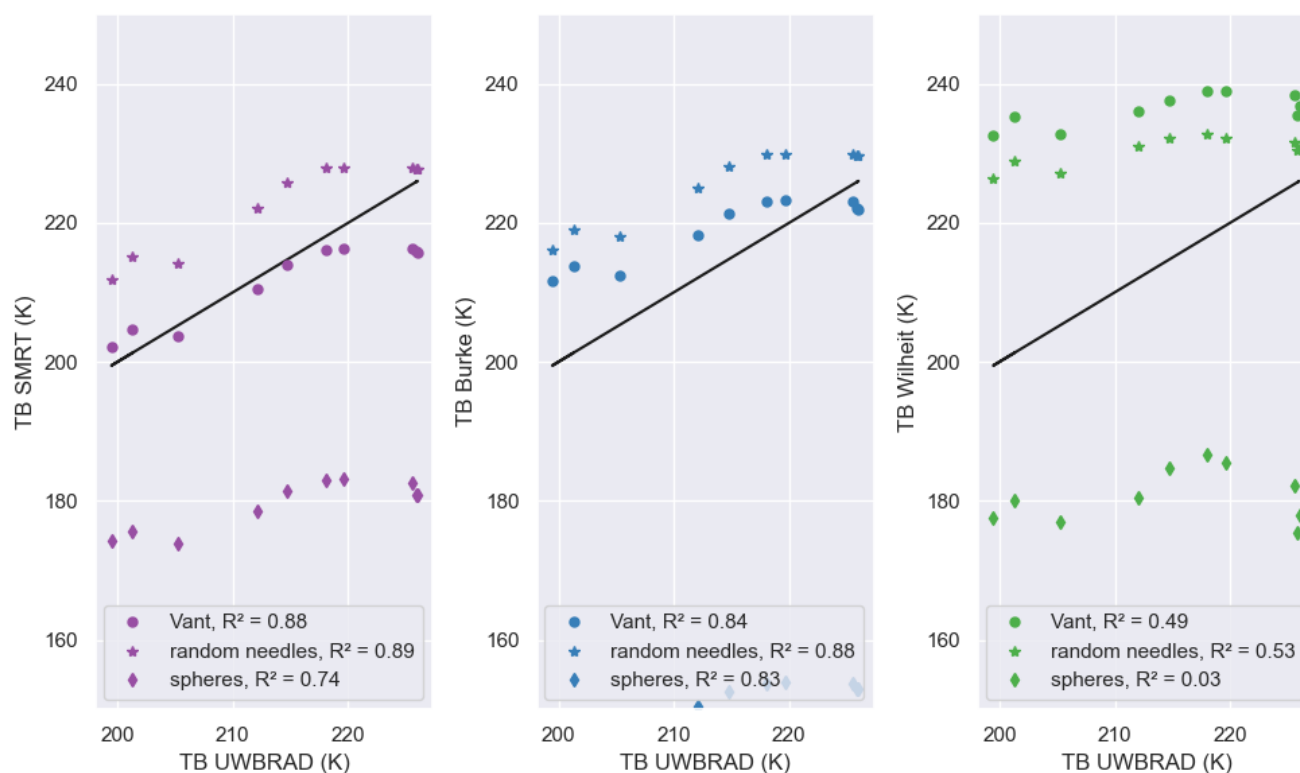


**Fig. 9.** Scatter plots of the brightness temperature modeled with the different configurations as function of the UWBRAD's first period measurements, along with their respective correlation coefficient.

333 Figure 8 shows the relative difference of comparing the modeled brightness temperature using different  
 334 models and permittivity formulations with the UWBRAD in situ measurements during late 2019, from  
 335 4th to 13th December. All configurations using the Burke and SMRT models combined with the Vant or  
 336 the random needles formulations present similar metrics, as expected from Figure 4. However, the Vant  
 337 permittivity is slightly superior compared to the random needles, and the same can be argued for SMRT  
 338 compared to Burke.

339 Figure 9 shows the scatter plots for each model with the different permittivities. The  $R^2$  coefficients are  
 340 good, except for the Wilheit model. Again the configurations combining the Burke or the SMRT models  
 341 with the Vant or the random needles permittivity are proven to be superior above the others. The spheres  
 342 permittivity results in extremely lower brightness temperatures which are not physical for sea ice, specially  
 343 when combined with the Burke model.

344 In Demir and others (2022a), a good match is found between UWBRAD measurements in this period and  
 345 a multilayer, incoherent radiative transfer model that includes a snow layer, a second year ice layer (given

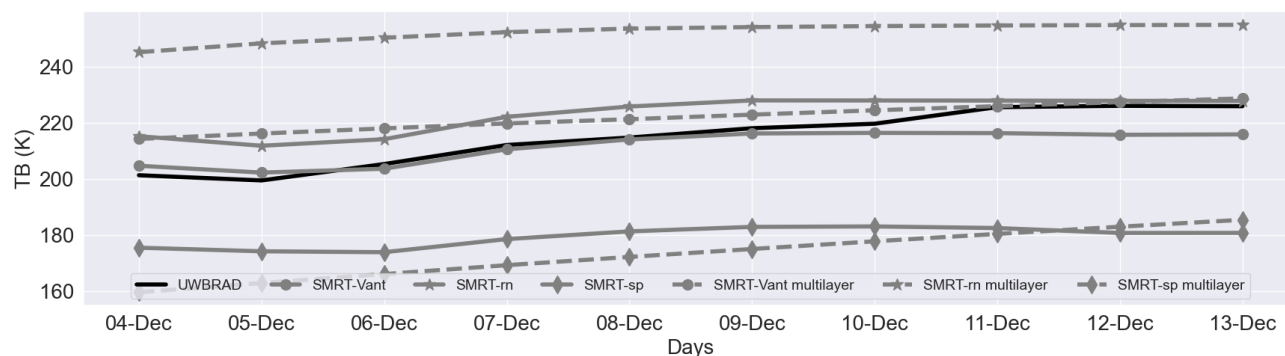


**Fig. 10.** Temporal evolution of the UWBRAD brightness temperature modeled with the combination of the CFDD simulation and the SMRT model considering different permittivities, along with the model approach proposed in Demir and others (2022a) denoted as *multilayer*.

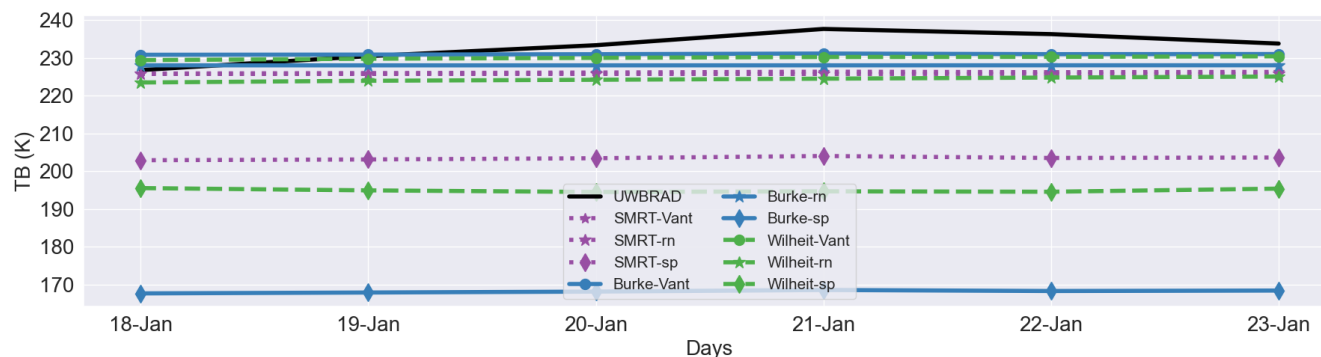


**Fig. 11.** Temporal evolution of the brightness temperature modeled with the combination of the CFDD simulation and the Burke, SMRT and Wilheit models, along with the UWBRAD's second period measurements.

346 the low salinity of the upper ice column, 0.4), a first year layer to model the measured accretion of ice to  
 347 the base of the column, and the ocean. Ice growth from about 67 cm to 78 cm was observed during the  
 348 coincident DTC observations. Taking advantage of SMRT's capacity to consider multiple layers, 10 shows  
 349 the approach employed in this study and compares it with the approach suggested in Demir and others  
 350 (2022a). The latter involves the incorporation of a saline first-year ice layer underneath a desalinated  
 351 thicker layer, assumed to be growing up to 8.3 cm during the studied period. The TB increasing trend is  
 352 similarly well reproduced by both approaches, indicating that it can be reproduced either by the increase  
 353 in depth of the saline layer, or considering only one ice layer with a salinity approaching the average of  
 354 both the desalinated and growing saline layers.

355

356

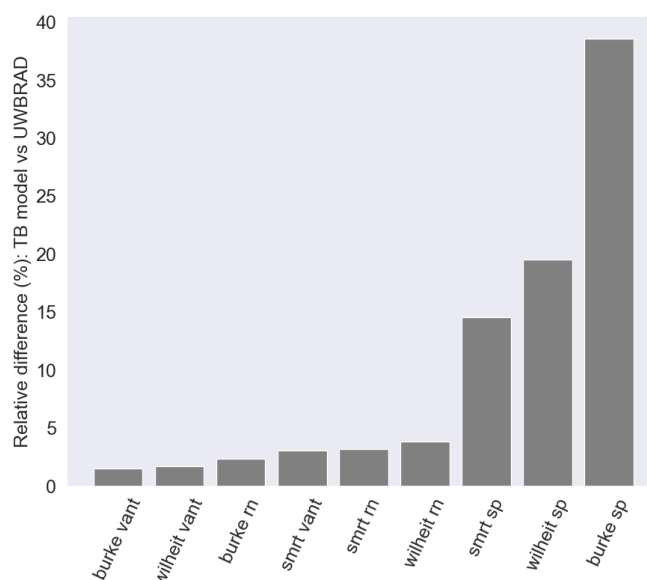


**Fig. 12.** Relative difference of the modeled brightness temperature from the Burke, SMRT and Wilheit models assuming different permittivities with respect to the in situ UWBRAD measurements during the second period.

357 For the early winter UWBRAD measurements, from 18th to 23rd January, the temporal evolution is  
 358 presented in 11. In this period the instruments measured at a fixed incidence angle of  $35^{\circ}$ C, and the  
 359 modeled TB is also integrated over the whole antenna pattern as done for the first period. The models  
 360 are not able to follow the trend observed by the instrument, although the values are similar. It can be  
 361 hypothesized that, as in January the ice is more consolidated and thus thicker than 1 m, as seen in 3, it is  
 362 out of the sensitivity range of the models at this frequency band. Here again the Burke and SMRT models  
 363 are almost equivalent, except when the sphere permittivity model is used for which the SMRT is much  
 364 better than the others.

365 Figure 12 shows the relative difference of the different model configurations compared to the measured  
 366 UWBRAD data for this period. The differences remain similar to those for early December, as well as the  
 367 best model configurations, although the results are close between all the models assuming pure random  
 368 needles or the Vant formulation. Figure 13 provides scatter plots of the presented models with the different  
 369 permittivity formulations. The Vant and random needles formulation are better than spheres, but in any  
 370 case reproducing the observed trend. Despite that, for this period the thickness variability is smaller, so the  
 371 uncertainty introduced by using the ice coring combined with the CFDD model can result in the observed  
 372 deviation. This argument can be further enhanced by the fact that the relative differences shown in 12 are  
 373 in the range 0 – 10 %, thus being reasonably good compared to the  $R^2$  metrics. The sample may be too

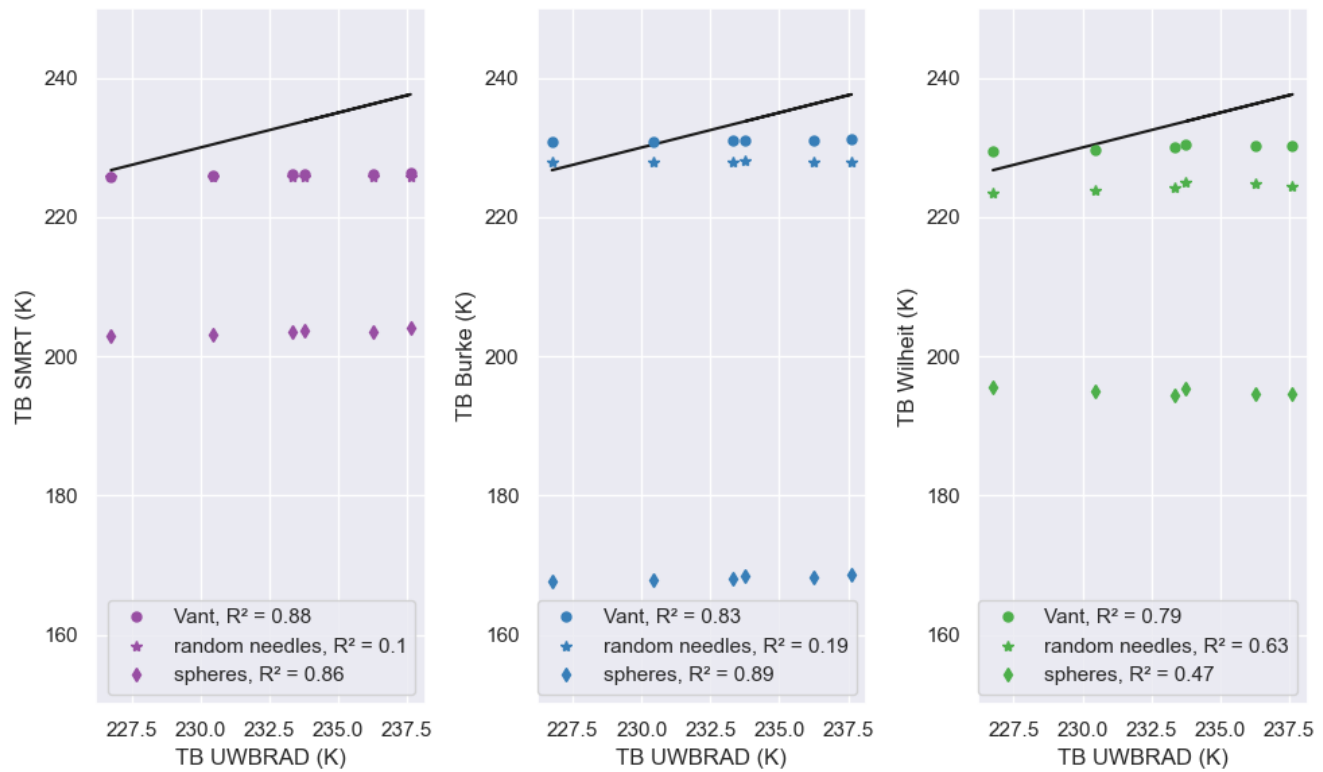


**Fig. 13.** Scatter plots of the brightness temperature modeled with the different configurations as function of the UWBRAD's second period measurements, along with their respective correlation coefficient.



374 small to confirm this hypothesis, as it also could be due to sensitivity saturation for thicker ice, as pointed  
375 out previously.

## 376 5 DISCUSSION

377 Starting with the sea ice growth simulation using the CFDD model, there is an overestimation of the  
378 sea ice thickness compared to the simulation with some ice coring profiles, and an underestimation of  
379 around 5 to 10 cm compared to the DTC data. These discrepancies can enlarge the difference of the  
380 posterior computation of the brightness temperature using the radiative transfer models. This is reasonable  
381 considering the simplicity of the model, as it only accounts for the growing and neither melting nor decrease  
382 of the thickness is possible. The CFDD-simulated sea ice temperature is clearly deviated from the ground  
383 truth observations, presenting a similar trend but much lower bulk temperatures, of around 5 to 10 °C less.  
384 This can be associated to the insulation effect of the snow above ice. The DTC-derived temperature remains  
385 much closer to the ice coring, justifying its use in the modeled brightness temperature computation. The  
386 sea ice salinity is slightly deviated, but the trend seems to be well reproduced being constant. Therefore,  
387 the major source of uncertainty in this case is the sea ice temperature, due to its observed variability. It  
388 can present a wide range of values producing an important impact in the TB, while the sea ice salinity is  
389 shown to be almost constant and the thickness is well reproduced by a common growth for that time of  
390 the year.

391 Regarding the radiometric data analysis, it is remarkable that for almost every period the different radiative  
392 transfer models obtain similar results when assuming the same permittivity formulation. Namely, the  
393 permittivity modeling seems to have a greater impact on the output brightness temperature than the  
394 approach, incoherent or coherent, of the radiative model. Noteworthy, although assuming spherical brine  
395 inclusions results in an unrealistic permittivity, an important difference between combining it with the  
396 SMRT model compared to the others is shown. Furthermore, the coherence effects included in the in  
397 the Wilheit model also lead to better results than the Burke model, probably because greater brightness  
398 temperatures can be reached with the model's predicted phase oscillations, as shown in 1, although these  
399 oscillations are not evident in the measurements. Despite the fact that the scattering is negligible at this  
400 low frequency, Burke model predicted brightness temperatures remain lower than those of the SMRT. It  
401 can be hypothesized that it is because the Burke model misses a fundamental contribution to the emission  
402 which involves the snow layer. Specifically, it does not account for the radiation coming from the ice being

403 reflected from the snow bottom and then re-reflected again at the snow bottom that is finally transmitted  
404 through the snow top. The effect of neglecting these high order reflections is enhanced when considering  
405 the spheres formulation, as the difference with SMRT is much higher. This results in an average difference  
406 between Burke and SMRT of around 30 K when assuming spheres, while is kept below 5 K when random  
407 needles or Vant is used.

408 Figures 4, 7 and 11 suggest that, except for TBH measured by ELBARA during the sea ice growth period,  
409 where no model is able to well reproduce the in situ data, the in situ values lay within the region between  
410 each model's result when considering spheres and random needles. As one could expect, this indicates that  
411 the optimal permittivity should be somewhere between these theoretical formulations. The situation where  
412 the brine inclusions are perfect spheres or randomly-oriented needles, or even homogeneous, seems to be  
413 unrealistic for the naturally grown sea ice, and thus it could make sense to model them as imperfect and  
414 heterogeneous. Additionally, although the Vant formulation could be seen as the appropriate permittivity  
415 to be used as it was empirically derived and presents robust results as shown, its coefficients are interpolated  
416 to L-band and thus uncertainty is introduced.

417 Significant oscillations in the Wilheit model, particularly when paired with the spheres formulation, are  
418 evident in (4, but not in 7 and 11). For the latter, it can be hypothesized that the oscillations are averaged  
419 out by integrating the model predictions for the different incidence angles over the UWBRAD antenna  
420 pattern. These oscillations are because of the coherence effects considered in this model, as illustrated in  
421 1. The choice of permittivity seems to be linked to these jumps, with the spheres and Vant formulations  
422 displaying oscillations across a wider range of sea ice conditions (see 1). Again it is noted that no clear  
423 evidence of oscillatory behaviors in the measured brightness temperatures is observed.

424 The modeled brightness temperature for UWBRAD's first period presents great agreement with the in situ  
425 observations, following the TB increasing trend when considering almost every model configuration, except  
426 those with the Wilheit model or the spheres permittivity. This suggests that, even though the models were  
427 driven by sparsely sampled physical property measurements, the problem of infrequent time sampling is  
428 partially addressed using frequent DTC temperature sensor strings embedded in the ice, providing frequent  
429 temperature profile data. Moreover, once the temperature reaches the melting point, the ice thickness can  
430 be inferred. Salinity measurements over time are less frequent as weekly core data were used. In Demir  
431 and others (2022a), similarly to this paper's analysis, the model was applied to the time varying physical  
432 properties, obtaining also a good agreement between the model and the brightness temperature for the

433 period from December 4 to December 14 (see Figure 10 in Demir and others (2022a)). Therefore, the two  
434 different approaches to the sea ice layering model lead to similar great results.  
435 Finally, Figure 3 indicates that the ice in the UWBRAD's early winter period was thicker than 1 m, for  
436 which the models at this frequency may not have sensitivity, as the saturation zone (see Figure 1) may  
437 have been reached given the ice conditions. However, the results could be acceptable considering that the  
438 sample is too small to observe any trend, producing a bias in the correlation coefficient. This is enhanced  
439 by Figure 12, which generally shows small relative differences for the modeled brightness temperatures,  
440 except when considering the spheres permittivity formulation.

## 441 6 CONCLUSIONS

442 The MOSAiC expedition was a unique opportunity to gather valuable data about the Arctic environment.  
443 Specially, the data collected by the L-band radiometers such as ELBARA and UWBRAD, can help to  
444 improve understanding of sea ice emission modeling which is key for the retrieval of geophysical parameters  
445 using remote sensing observations. The data from these instruments have been successfully handled to  
446 perform a comparison with three different radiative transfer models, in combination with three distinct  
447 permittivity formulations. From this analysis, multiple conclusions can be extracted.

448 Regarding the analysis using different radiative transfer models, it is shown that Burke and SMRT present  
449 a similar behavior as scattering can be neglected at a low frequency such as L-band. Nevertheless, the  
450 Burke model is seen to be strictly lower as it does not include the contributions to the emission from  
451 higher order reflections that happen within the snow-ice interface. This is highly enhanced when both  
452 models consider the spheres permittivity, as a more important difference between them appears, reaching  
453 up to 25 K more than when random needles or Vant is considered. The coherent approach used in the  
454 Wilheit model is the only approach capable of reproducing the high TBH values, even the larger than  
455 TBV observed by ELBARA in the first days of the sea ice growth period. Although it can be argued that  
456 this unusual high values are not physically realistic, for the other periods where the TBH measurements  
457 are nominal and generally the models predict lower values, the Wilheit model presents the most similar  
458 results. While this may suggest the presence of coherent effects, the oscillatory brightness temperatures that  
459 would result are not clearly observed in the measurements. Nevertheless, when modeling the UWBRAD  
460 measurements there is no major distinction between the two approaches. It can be said that incoherent  
461 models show slight better results for the vertical polarization, but poorer at the horizontal component and

462 so at intensity overall.

463 Focusing on the permittivity modeling, the widely used Vant empirical formulation is shown to be a robust  
464 option, as it presents reasonable results in every period, both for ELBARA and UWBRAD. However, for  
465 the ELBARA measurements specifically, the random needles formulation has better metrics. Assuming the  
466 brine inclusions as perfect spherical inclusions results in an unrealistic behavior on reproducing the in situ  
467 radiometric measurements. Ultimately, this study suggest that the more realistic permittivity lays within  
468 the range between the spheres and the random needles formulation, for which future field measurements  
469 can help in order to derive a new empirical formulation specifically for L-band.

470 In summary, these findings have implications for sea ice emission modeling and highlight the need for  
471 more in situ measurements to improve the current permittivity formulations, along with the importance of  
472 considering the coherence effects that are currently neglected at L-band remote sensing applications.

## 473 **7 ACKNOWLEDGMENTS**

474 This project is funded from the AEI with the ARCTIC-MON project (PID2021-125324OB-I00) and also  
475 with the Programación Conjunta Internacional project called "MEJORANDO LOS MODELOS DE EMI-  
476 SIVIDAD DEL HIELO MARINO EN LAS MICROONDAS DE BAJA FRECUENCIA" (ICE-MOD), with  
477 reference PCI2019-111844-2. This work represents a contribution to the CSIC Thematic Interdisciplinary  
478 Platform PTI-POLARCSIC and PTI-TELEDETECT and is supported by the Spanish government through  
479 the "Severo Ochoa Centre of Excellence" accreditation (CEX2019-000928-S).

480 **REFERENCES**

- 481 Angelopoulos M, Damm E, Simões Pereira P, Abrahamsson K, Bauch D, Bowman JS, Dumitrascu A, Marsay CM,  
482 Rinke A, Sachs T, Stefels J, Stephens M, Verdugo J, Wang L and Zhan L (2022) Physical properties of sea ice cores  
483 from site BGC1 measured on legs 1 to 3 of the MOSAiC expedition. PANGAEA (doi: 10.1594/PANGAEA.943768)
- 484 Angelopoulos M, Damm E, Simões Pereira P, Abrahamsson K, Bauch D, Bowman J, Castellani G, Creamean J,  
485 Divine DV, Dumitrascu A, Fons SW, Granskog MA, Kolabutin N, Krumpfen T, Marsay C, Nicolaus M, Oggier M,  
486 Rinke A, Sachs T, Shimanchuk E, Stefels J, Stephens M, Ulfso A, Verdugo J, Wang L, Zhan L and Haas C (2022)  
487 Deciphering the Properties of Different Arctic Ice Types During the Growth Phase of MOSAiC: Implications for  
488 Future Studies on Gas Pathways. *Frontiers in Earth Science*, **10**, ISSN 2296-6463 (doi: 10.3389/feart.2022.864523)
- 489 Assur A (1960) Composition of sea ice and its tensile strength. Technical report, Technical report, U.S. Army Snow,  
490 Ice and Permafrost Research Establishment, Wilmette, Ill
- 491 Bilello M (1961) Formation, growth, and decay of sea-ice in the Canadian Arctic Archipelago. *Arctic*
- 492 Burke W, Schmugge T and Paris J (1979) Comparison of 2.8- and 21-cm microwave radiometer obser-  
493 vations over soils with emission model calculations. *Journal of Geophysical Research*, **84**, 287–294 (doi:  
494 <https://doi.org/10.1029/JC084iC01p00287>)
- 495 Cox GFN and Weeks WF (1988) Numerical simulations of the profile properties of undeformed first-year  
496 sea ice during the growth season. *Journal of Geophysical Research: Oceans*, **93**(C10), 12449–12460 (doi:  
497 <https://doi.org/10.1029/JC093iC10p12449>)
- 498 Demir O and Johnson J (2021a) Arctic Sea Ice Thermal Emission Measurements from the Ultra Wideband Microwave  
499 Radiometer (UWBRAD) at the Multidisciplinary Drifting Observatory for the Study of Arctic Climate (MOSAiC)  
500 Expedition in December 2019. Arctic Data Center (doi: 10.18739/A2M03XZ32)
- 501 Demir O and Johnson J (2021b) Arctic Sea Ice Thermal Emission Measurements from the Ultra Wideband Microwave  
502 Radiometer (UWBRAD) at the Multidisciplinary Drifting Observatory for the Study of Arctic Climate (MOSAiC)  
503 Expedition in January 2020. Arctic Data Center (doi: 10.18739/A2G737506)
- 504 Demir O, Johnson JT, Jezek KC, Andrews MJ, Ayotte K, Spreen G, Hendricks S, Kaleschke L, Oggier M, Granskog  
505 MA, Fong A, Hoppmann M, Matero I and Scholz D (2022a) Measurements of 540–1740 MHz Brightness Temper-  
506 atures of Sea Ice During the Winter of the MOSAiC Campaign. *IEEE Transactions on Geoscience and Remote*  
507 *Sensing*, **60**, 1–11 (doi: 10.1109/TGRS.2021.3105360)

- 508 Demir O, Johnson JT, Jezek KC, Brogioni M, Macelloni G, Kaleschke L and Brucker L (2022b) Studies of Sea-Ice  
509 Thickness and Salinity Retrieval Using 0.5–2 GHz Microwave Radiometry. *IEEE Transactions on Geoscience and*  
510 *Remote Sensing*, **60**, 1–12 (doi: 10.1109/TGRS.2022.3168646)
- 511 Doronin Y (1971) *Thermal interaction of the atmosphere and the hydrosphere in the Arctic*. Coronet Books, Philadel-  
512 phia
- 513 Entekhabi D, Njoku EG, O'Neill PE, Kellogg KH, Crow WT, Edelstein WN, Entin JK, Goodman SD, Jackson TJ,  
514 Johnson J, Kimball J, Piepmeier JR, Koster RD, Martin N, McDonald KC, Moghaddam M, Moran S, Reichle R,  
515 Shi JC, Spencer MW, Thurman SW, Tsang L and Van Zyl J (2010) The Soil Moisture Active Passive (SMAP)  
516 mission. *Proceedings of the IEEE*, **98** (5), 704–716
- 517 Font J, Camps A, Borges A, Martin-Neira M, Boutin J, Reul N, Kerr Y, Hahne A and Mecklenburg S (2010) SMOS:  
518 The challenging sea surface salinity measurement from space. *Proceedings of the IEEE*, **98**(5), 649–665, ISSN  
519 0018-9219 (doi: 10.1109/JPROC.2009.2033096)
- 520 Gabarró C, Fabregat P, Hernández-Macià F, Jove R, Salvador J, Spreen G, Thielke L, Dadic R, Huntemann M,  
521 Kolabutin N, Nomura D, Hannula HR and Schneebeli M (2022) First results of the ARIEL L-band radiometer on the  
522 MOSAiC Arctic Expedition during the late summer and autumn period. *Elementa: Science of the Anthropocene*,  
523 **10**(1), ISSN 2325-1026 (doi: 10.1525/elementa.2022.00031), 00031
- 524 Hersbach H, Bell B, Berrisford P, Biavati G, Horányi A, Muñoz Sabater J, Nicolas J, Peubey C, Radu R, Rozum I,  
525 Schepers D, Simmons A, Soci C, Dee D and Thépaut JN (2020) ERA5 hourly data on single levels from 1940 to  
526 present. Copernicus Climate Change Service (C3S) Climate Data Store (CDS) (doi: 10.24381/cds.adbb2d47)
- 527 Heygster G, Huntemann M, Ivanova N, Saldo R and Pedersen LT (2014) Response of passive microwave sea ice  
528 concentration algorithms to thin ice. In *2014 IEEE Geoscience and Remote Sensing Symposium*, 3618–3621 (doi:  
529 10.1109/IGARSS.2014.6947266)
- 530 Huntemann M (2015) *Thickness retrieval and emissivity modeling of thin sea ice at L-band for SMOS satellite*  
531 *observations*. Ph.D. thesis
- 532 Huntemann M, Heygster G, Kaleschke L, Krumpfen T, Mäkynen M and Drusch M (2014) Empirical sea ice thickness  
533 retrieval during the freeze-up period from SMOS high incident angle observations. *The Cryosphere*, **8**, 439–451  
534 (doi: <https://doi.org/10.5194/tc-8-439-2014>)
- 535 Jezek KC, Johnson JT, Demir O, Andrews MJ, Macelloni G, Brogioni M, Leduc-Leballeur M, Tan S, Tsang L,  
536 Kwok R, Kaleschke L, Belgiovane DJ, Chen CC and Bringer A (2019) Remote Sensing of Sea Ice Thickness and  
537 Salinity With 0.5–2 GHz Microwave Radiometry. *IEEE Transactions on Geoscience and Remote Sensing*, **57**(11),  
538 8672–8684 (doi: 10.1109/TGRS.2019.2922163)

- 539 Johnson JT, Jezek KC, Aksoy M, Bringer A, Yardim C, Andrews M, Chen CC, Belgiovane D, Leuski V, Du-  
540 rand M, Duan Y, Macelloni G, Brogioni M, Tan S, Wang TL and Tsang L (2016) The Ultra-wideband  
541 Software-Defined Radiometer (UWBRAD) for ice sheet internal temperature sensing: Results from recent ob-  
542 servations. In *2016 IEEE International Geoscience and Remote Sensing Symposium (IGARSS)*, 7085–7087 (doi:  
543 10.1109/IGARSS.2016.7730848)
- 544 Kaleschke L, Tian-Kunze X, Maaß N, Mäkynen M and Drusch M (2012) Sea ice thickness retrieval from SMOS bright-  
545 ness temperatures during the Arctic freeze-up period. *Geophysical Research Letters*, doi:10.1029/2012GL050916
- 546 Kerr Y, Waldteufel P, Wigneron J, Delwart S, Cabot F, Boutin J, Escorihuela M, Font J, Reul N, Gruhier C, Juglea S,  
547 Drinkwater M, Hahne A, Martin-Neira M and Mecklenburg S (2010) The SMOS mission: New tool for monitoring  
548 key elements of the global water cycle. *Proceedings of the IEEE IGARSS 2010, no. 5.*, **98**, 666–687
- 549 Klein L and Swift C (1977) An improved model for the dielectric constant of sea water at microwave frequencies.  
550 *IEEE Transactions on Antennas and Propagation*, **AP-25**(1), 104–111
- 551 Kwok R (2018) Arctic sea ice thickness, volume, and multiyear ice coverage: losses and coupled variability  
552 (1958–2018). *Environmental Research Letters*, **13**(10), 105005 (doi: 10.1088/1748-9326/aae3ec)
- 553 Maass N, Kaleschke L, Tian-Kunze X and Tonboe RT (2015) Snow thickness retrieval from L-band brightness  
554 temperatures: a model comparison. *Annals of Glaciology*, **56**(69), 9–17 (doi: 10.3189/2015AoG69A886)
- 555 Mecklenburg S, Wright N, Bouzina C and Delwart S (2009) Getting down to business - SMOS operations and  
556 products. *ESA Bulletin*, **137**, 25–30
- 557 Mätzler C (1996) Microwave permittivity of dry snow. *Geoscience and Remote Sensing, IEEE Transactions on*,  
558 **34**(2), 573–581, ISSN 01962892 (doi: 10.1109/36.485133)
- 559 Mätzler C (2006) *Thermal Microwave Radiation: Applications For Remote Sensing*, publisher = Institution Of  
560 *Electrical Engineers*
- 561 Naderpour R and Schwank M (2021) Sled-Mounted ELBARA-III in MOSAiC Expedition: Measurement and Data  
562 Processing Report. Technical report
- 563 Nakawo M and Sinha NK (1981) Growth Rate and Salinity Profile of First-Year Sea Ice in the High Arctic. *Journal*  
564 *of Glaciology*, **27**(96), 315–330 (doi: 10.3189/S0022143000015409)
- 565 Nicolaus M, Perovich DK, Spreen G, Granskog MA, von Albedyll L, Angelopoulos M, Anhaus P, Arndt S, Belter  
566 HJ, Bessonov V, Birnbaum G, Brauchle J, Calmer R, Cardellach E, Cheng B, Clemens-Sewall D, Dadic R, Damm  
567 E, de Boer G, Demir O, Dethloff K, Divine DV, Fong AA, Fons S, Frey MM, Fuchs N, Gabarró C, Gerland S,

- 568 Goessling HF, Gradinger R, Haapala J, Haas C, Hamilton J, Hannula HR, Hendricks S, Herber A, Heuzé C,  
569 Hoppmann M, Høyland KV, Huntemann M, Hutchings JK, Hwang B, Itkin P, Jacobi HW, Jaggi M, Jutila A,  
570 Kaleschke L, Katlein C, Kolabutin N, Krampe D, Kristensen SS, Krumpen T, Kurtz N, Lampert A, Lange BA,  
571 Lei R, Light B, Linhardt F, Liston GE, Loose B, Macfarlane AR, Mahmud M, Matero IO, Maus S, Morgenstern  
572 A, Naderpour R, Nandan V, Niubom A, Oggier M, Oppelt N, Pätzold F, Perron C, Petrovsky T, Pirazzini R,  
573 Polashenski C, Rabe B, Raphael IA, Regnery J, Rex M, Ricker R, Riemann-Campe K, Rinke A, Rohde J, Salganik  
574 E, Scharien RK, Schiller M, Schneebeli M, Semmling M, Shimanchuk E, Shupe MD, Smith MM, Smolyanitsky  
575 V, Sokolov V, Stanton T, Stroeve J, Thielke L, Timofeeva A, Tonboe RT, Tavri A, Tsamados M, Wagner DN,  
576 Watkins D, Webster M and Wendisch M (2022) Overview of the MOSAiC expedition: Snow and sea ice. *Elementa:  
577 Science of the Anthropocene*, **10**(1), ISSN 2325-1026 (doi: 10.1525/elementa.2021.000046), 000046
- 578 Picard G, Sandells M and Löwe H (2018) SMRT: an active–passive microwave radiative transfer model for snow with  
579 multiple microstructure and scattering formulations (v1.0). *Geoscientific Model Development*, **11**(7), 2763–2788  
580 (doi: 10.5194/gmd-11-2763-2018)
- 581 Salganik E, Hoppmann M, Scholz D, Haapala J and Spreen G (2023a) Temperature after the cooling cycle from the  
582 sea ice mass balance buoy DTC12 during MOSAiC 2019/2020. PANGAEA (doi: 10.1594/PANGAEA.962441), in:  
583 Salganik, E et al. (2023): Temperature and heating induced temperature difference measurements from the sea ice  
584 mass balance buoy DTC12 during MOSAiC 2019/2020. PANGAEA, <https://doi.org/10.1594/PANGAEA.962434>
- 585 Salganik E, Hoppmann M, Scholz D, Itkin P, Katlein C, Divine DV and Raphael I (2023b) Temperature after  
586 the cooling cycle from the sea ice mass balance buoy DTC20 during MOSAiC 2019/2020. PANGAEA (doi:  
587 10.1594/PANGAEA.962452), in: Salganik, E et al. (2023): Temperature and heating induced temperature dif-  
588 ference measurements from the sea ice mass balance buoy DTC20 during MOSAiC 2019/2020. PANGAEA,  
589 <https://doi.org/10.1594/PANGAEA.962450>
- 590 Schwank M, Wiesmann A, Werner C, Mätzler C, Weber D, Murk A, Völsch I and Wegmüller U (2010) ELBARA  
591 II, an L-Band Radiometer System for Soil Moisture Research. *Sensors*, **10**(1), 584–612, ISSN 1424-8220 (doi:  
592 10.3390/s100100584)
- 593 Shokr M (1998) Field observations and model calculations of dielectric properties of Arctic sea ice in the microwave  
594 C-band. *IEEE Transactions on Geoscience and Remote Sensing*, **36**(2), 463–478 (doi: 10.1109/36.662730)
- 595 Stogryn A and Desargant G (1985) The dielectric properties of brine in sea ice at microwave frequencies. *IEEE  
596 Transactions on Antennas and Propagation*, **33**(5), 523–532 (doi: 10.1109/TAP.1985.1143610)
- 597 Tiuri M, Sihvola A, Nyfors E and Hallikaiken M (1984) The complex dielectric constant of snow at microwave fre-  
598 quencies. *IEEE Journal of Oceanic Engineering*, **9**(5), 377–382, ISSN 0364-9059 (doi: 10.1109/JOE.1984.1145645)



- 599 Vant M, Ramseier R and Makios V (1978) The complex-dielectric constant of sea ice at frequencies in the range  
600 0.1–40 GHz. *Journal of Applied Physics*, **49**, 1264–1280
- 601 Warren SG, Rigor IG, Untersteiner N, Radionov VF, Bryazgin NN, Aleksandrov YI and Colony R  
602 (1999) Snow Depth on Arctic Sea Ice. *Journal of Climate*, **12**(6), 1814–1829 (doi: 10.1175/1520-  
603 0442(1999)012<1814:SDOASI>2.0.CO;2)
- 604 Weeks W (2010) *On Sea Ice*. University of Alaska Press, ISBN 9781602231016
- 605 Wilheit TT (1978) Radiative Transfer in a Plane Stratified Dielectric. *IEEE Transactions on Geoscience Electronics*,  
606 **16**(2), 138–143 (doi: 10.1109/TGE.1978.294577)

For Peer Review